




Lensfree on-chip microscopy based on single-plane phase retrieval: supplement

CHENG GUO,^{1,2,3,7} XIANMING LIU,³ FEILONG ZHANG,³  YONGBIN DU,^{1,2} SHENGHAO ZHENG,^{1,2} ZEHUA WANG,^{1,2} XIAOQING ZHANG,⁴ XINGCHI KAN,⁵ ZHENGJUN LIU,⁶  AND WEIBO WANG^{1,2,8} 

¹Center of Ultra-precision Optoelectronic Instrument Engineering, Harbin Institute of Technology, Harbin 150080, China

²Key Lab of Ultra-precision Intelligent Instrumentation (Harbin Institute of Technology), Ministry of Industry and Information Technology, Harbin 150080, China

³School of Computer Science and Technology, Harbin Institute of Technology, Harbin 150001, China

⁴School of Life Science and Technology, Harbin Institute of Technology, Harbin 150080, China

⁵College of Veterinary Medicine, Jilin University, Changchun 130062, China

⁶School of Physics, Harbin Institute of Technology, Harbin 150001, China

⁷guocheng_27@163.com

⁸wwbhit@hit.edu.cn

This supplement published with Optica Publishing Group on 19 May 2022 by The Authors under the terms of the [Creative Commons Attribution 4.0 License](https://creativecommons.org/licenses/by/4.0/) in the format provided by the authors and unedited. Further distribution of this work must maintain attribution to the author(s) and the published article's title, journal citation, and DOI.

Supplement DOI: <https://doi.org/10.6084/m9.figshare.19753003>

Parent Article DOI: <https://doi.org/10.1364/OE.458400>

Lensfree on-chip microscopy based on single-plane phase retrieval: supplemental document

The supplemental document is organized as follows:

- (1) The detailed derivation of Eq. (16) is given;
- (2) The simulation results are added, where the performance of our method on different diffractive distances and noise types is discussed;
- (3) The parameter tuning and denoiser selection of our method are given;
- (4) Our method is expanded to other imaging sensors, such as CCD and sCMOS cameras, to verify the robustness;
- (5) The experimental results that are not included in the manuscript, such as intestine and breast tissues, are supplemented;
- (6) The performance comparison of our method and multi-wavelength phase retrieval is added.

Derivation of Eq. (16)

The sub-problem in Eq. (16) can be solved by a cascade optimization, where the fidelity term and TV prior are successively processed as follows

$$g = \arg \min_{T^{k-1}} \left\| |A_Z T^{k-1}|^2 - I \right\|_2^2, \quad (\text{S1})$$

$$S = \arg \min_g \mu_1 \text{TV}(g). \quad (\text{S2})$$

Similar to the traditional phase retrieval framework, the fidelity term $\left\| |A_Z T^{k-1}|^2 - I \right\|_2^2$ can be minimized by an alternative projection

$$g = A_Z^H \left[\sqrt{I} \frac{A_Z T^{k-1}}{|A_Z T^{k-1}|} \right], \quad (\text{S3})$$

As for Eq. (S2), the minimization of TV term can be solved by a gradient descent form

$$S = \mu_1 \left(g - \gamma \frac{\partial \iint |\nabla g| dx dy}{\partial (g)^*} \right), \quad (\text{S4})$$

where γ is a step size for gradient descent algorithm. With the help of Euler-Lagrange equation [1, 2], the closed-form of the partial derivative is expressed as

$$\begin{aligned} \frac{\partial \iint |\nabla g| dx dy}{\partial (g)^*} &= \frac{\partial \sqrt{|\nabla_x g|^2 + |\nabla_y g|^2}}{\partial (g)^*} - \nabla \cdot \left[\frac{\partial \sqrt{|\nabla_x g|^2 + |\nabla_y g|^2}}{\partial [\nabla(g)^*]} \right] \\ &= \frac{\partial \sqrt{\nabla(g) \nabla[(g)^*]}}{\partial (g)^*} - \nabla \cdot \left[\frac{\partial \sqrt{\nabla(g) \nabla[(g)^*]}}{\partial [\nabla(g)^*]} \right] \\ &= -\frac{1}{2} \nabla \cdot \left[\frac{\nabla g}{|\nabla g|} \right]. \end{aligned} \quad (\text{S5})$$

Thus, the Eq. (S4) is expressed as

$$S = \frac{\mu_1}{2} \left[g + \frac{\gamma}{2} \nabla \cdot \left(\frac{\nabla g}{|\nabla g|} \right) \right]. \quad (\text{S6})$$

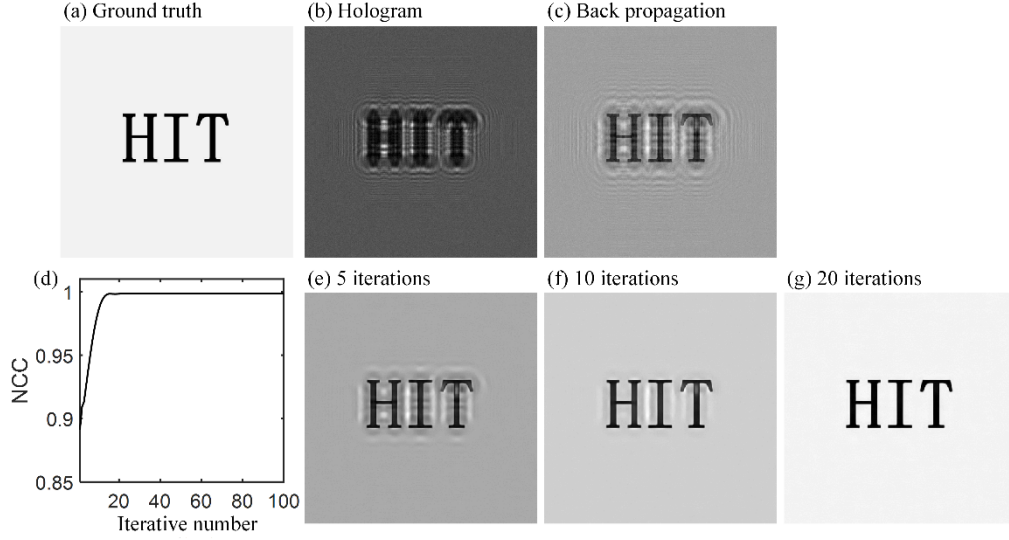


Fig. S1. Simulation results of 'HIT' target.

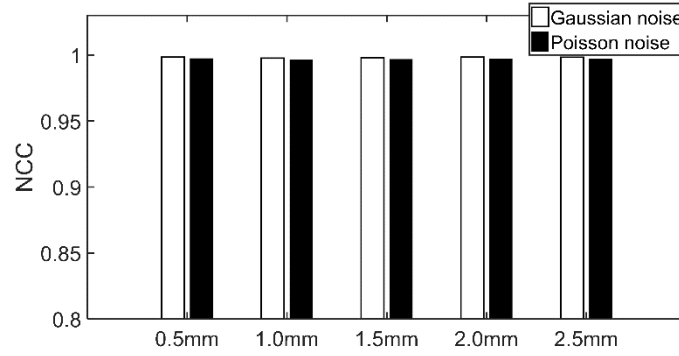


Fig. S2. The histogram of NCC values for different distance intervals

Simulation results

The simulation results of our method are presented in Fig. S1. Fig. S1(a) is set as a ground truth image. The simulated parameters are listed as follows: (1) the amplitude of object is Fig. S1(a), and the phase is a constant value; (2) the imaging size is 400 by 400, and the pixel size is $1.34\mu\text{m}$; (3) the wavelength is 532nm ; (4) the diffractive distance from sample to sensor plane is 0.75mm ; (5) Gaussian noise with a variance of 0.5 and Poisson noise with photon number of 10^6 are imposed in the imaging process. The simulated hologram and back-propagated image are shown in Fig. S1(b) and Fig. S1(c). The NCC metric (Normalized correlation coefficient) is used to assess the reconstructed accuracy, and its NCC curve is plotted in Fig. S1(d). The retrieved amplitude images with 5, 10, and 20 iterations are displayed in Figs. S1(e-g), where the twin-image artifacts are mitigated with the increase of iterative number. As the diffractive distances are set as 0.5mm, 1mm, 1.5mm, 2mm, and 2.5mm, the NCC values of retrieved images are displayed in Fig. S2. It is noted that our method is insensitive to distance range, which enables a noise-robust image reconstruction.

Parameter tuning and denoiser selection

We provide the process of parameter tuning and denoiser selection for our method. The estimation of noise variance is a key factor for joint denoising. An inaccurate guess of variance could remove much more detailed content. Thus, the variance of denoiser should be tuned to keep a balance of noise removal and resolution loss. In the portable system, a noise-free image cannot be obtained. Thus, we utilize a reference-free image assessment metric, contrast-to-noise ratio (CNR) [3], to find the optimal value of noise variance. In this process, a series of sample images are reconstructed by setting different denoising variances σ . Then, the reconstructed images are assessed by the CNR metric to form a CNR curve, where the biggest value point to the optimal parameter. The CNR metric is calculated as follows

$$\text{CNR} = \frac{|\langle S_b \rangle - \langle S_c \rangle|}{\text{std}(S_b)}, \quad (\text{S7})$$

where S_b and S_c denote background and object regions of reconstructed amplitude image. $\langle \cdot \rangle$ and 'std' represent mean value and standard deviation of the selected regions. The background and object regions can be extracted by imposing a threshold segmentation on the amplitude image.

Here a resolution target (Coherent Optics) is used for parameter tuning and denoiser selection. As an example, the CNR curve of TNRD filter is plotted in Fig. S3(a). As the variance σ is set as 0.001, 0.004, and 0.008, the retrieved targets are shown in Figs. S3(c-d). Note that the noisy artifact still exists in Fig. S3(c) but is removed in Fig. S3(d) and Fig. S3(e). However, in Fig. S3(e), a bigger variance leads to an over-denoising, which wipes out the high-frequency content. The visual judgment of Figs. S3(c-e) accords with the trend of the CNR curve. Therefore, we select $\sigma=0.004$ for TNRD filtering. The parameter tuning of the CS method is also finished by CNR metric.

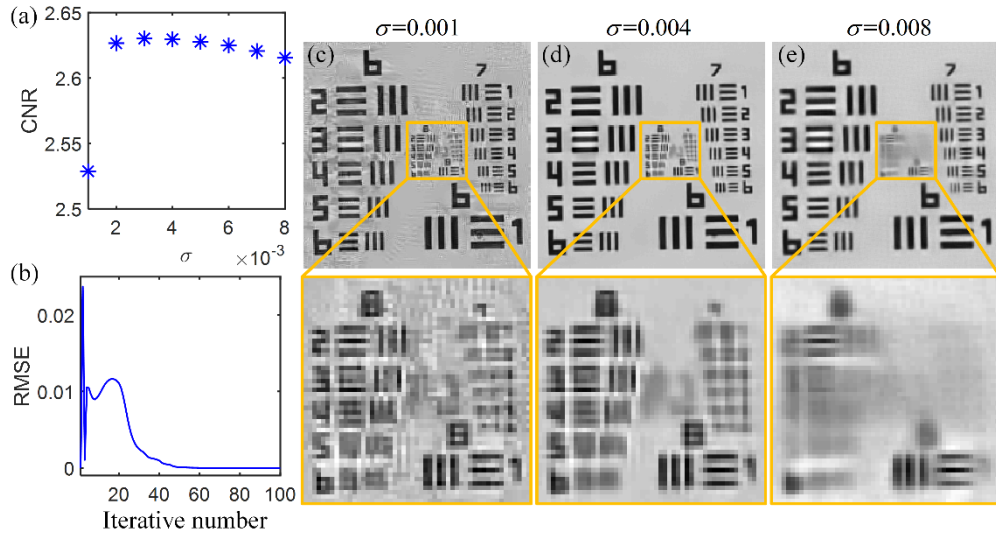


Fig. S3. The parameter tuning of denoising variance and iterative number for our method.

We utilize a relative means square error metric (RMSE) [4] to determine the stop criterion of iteration, and RMSE metric is defined as

$$\text{RMSE} = \frac{1}{M_0 \times N_0} \sum_{\forall m_0, n_0} \|T^{k+1} - T^k\|^2. \quad (\text{S8})$$

For TNRD filter, the RMSE versus iterative number is plotted in Fig. S3(b). It is noted that RMSE curve starts to be flat when the iterative number is larger than 50. Therefore, we set 50 iterations for image recovery.

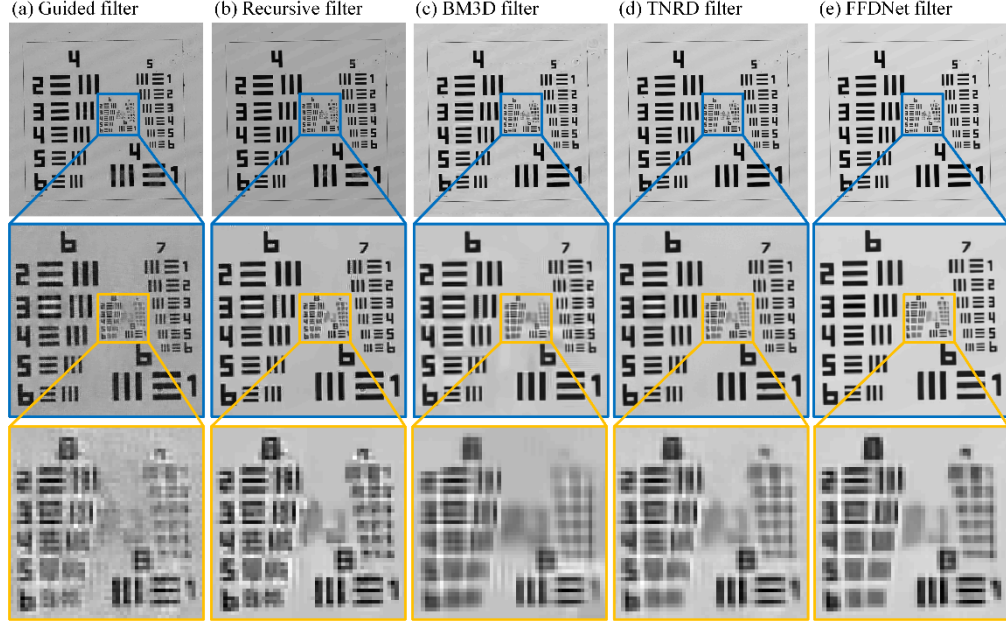


Fig. S4. The holographic reconstruction of resolution target using single-frame raw hologram with different image filters.

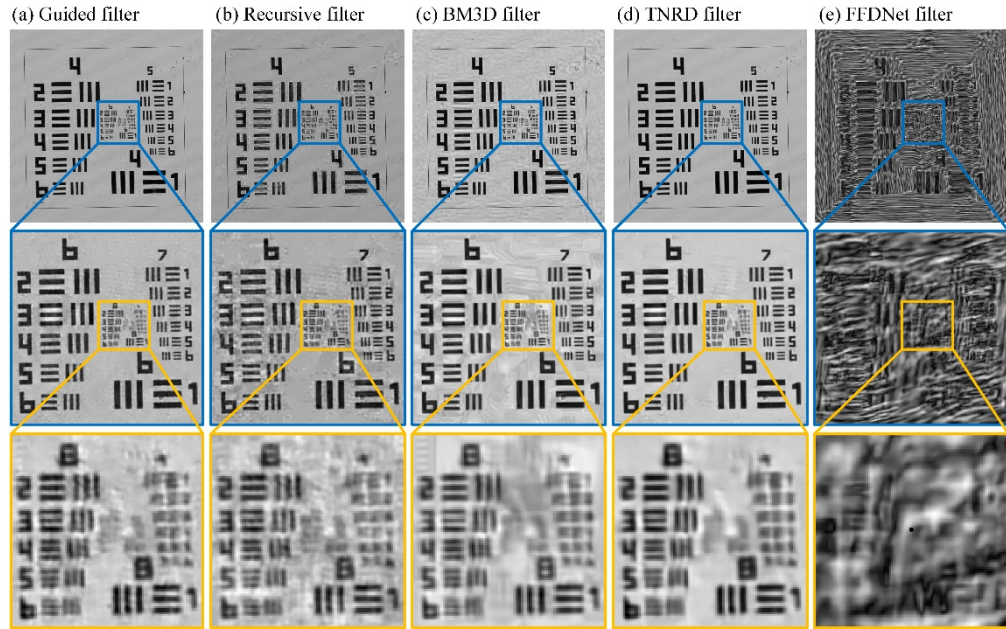


Fig. S5. The holographic reconstruction of resolution target using single-frame interpolated hologram with different image filters.

After parameter tuning, the optimal denoising values of BM3D filter, guided filter, TNRD filter, FFDNet, and recursive filter are listed in the Tab. S1. With the above parameters, the

resolution targets using different image filters are retrieved in Fig. S4. In Fig. S4(a) and Fig. S4(b), the results of guided and recursive filters have a little noisy artifact in the background. Especially for Group 8, the noise around the target cannot be removed. As shown in Figs. S4(c-e), the other three filters contribute a better imaging contrast. The resolution target used for calculation has a size of 1024×1024 . The running time of Figs. S4(a-e) is 22s、303s、132s、774s, and 917s, where all computation is executed on a laptop (CPU: AMD R7, RAM: 32GB, GPU : NVIDIA GeForce RTX3070). To show a further comparison, we offer the retrieved results of interpolated hologram in Fig. S5, where the hologram of resolution target is expanded to 2048×2048 by bicubic interpolation with an un-sampling factor of 2. In Fig. S5(e), the result of FFDNet filter is heavily distorted, which means that FFDNet filter is sensitive to parameter tuning and should be tuned again for another task. For Figs. S5(a-d), the best imaging quality is achieved by TNRD filter. As a result, guided filter is time-efficient, and TNRD filter owns the best image quality. In this paper, we assign TNRD filter for joint denoising of real and imaginary parts.

Table. S1 Optimal parameters of different image filters

Denoiser type	Parameter	Range of intensity image
Guided filter	Smooth value is 0.1	Intensity image should be normalized to a range from 0 to 255 for all methods
Recursive filter	Variance is 0.6	
BM3D filter	Variance is 0.004	
TNRD filter	Variance is 0.004	
FFDNet	Variance is 0.95	

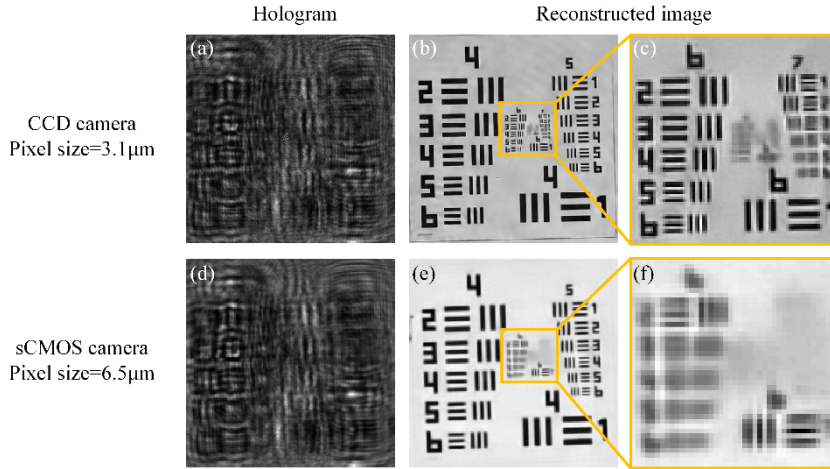


Fig. S6. The holographic reconstruction of resolution target using CCD and sCMOS cameras.

Single-frame imaging using CCD and sCMOS camera

We also expand our method to other cameras to perform lensless holographic reconstruction. Here two imaging sensors are used, including CCD (Point grey, GS3-US-41S4M-C, $3.1\mu\text{m}$) and sCMOS (PCO, edge 4.2LT, $6.5\mu\text{m}$) cameras. The two cameras both have the protecting package, thus the sample-to-sensor distances are larger than that of the on-chip system. The captured single-frame holograms from CCD and sCMOS cameras are shown in Fig. S6(a) and Fig. S6(d), where the corresponding sample-to-sensor distances are calibrated as 21.95mm and 23.73mm. The retrieved images related to CCD and sCMOS cameras are given in Figs. S6(b-c) and Figs. S6(e-f). It is noted that the imaging resolution of lensless holographic system is ultimately limited by the pixel size of the sensor. The smallest resolved elements of Fig. S6(c)

and Fig. S6(f) are element 2 of Group 7 and element 2 of Group 6, whose half-pitch resolutions are specified as $3.48\mu\text{m}$ and $6.96\mu\text{m}$. Considering that the pixel sizes of CCD and sCMOS cameras are $3.1\mu\text{m}$ and $6.5\mu\text{m}$, the imaging resolution of our method reaches the physical limit of CCD and sCMOS sensors. The results of Fig. S6 indicate that our method achieves a robust holographic image recovery, which is still feasible with different types of imaging sensors.

Image reconstruction of pathological slides

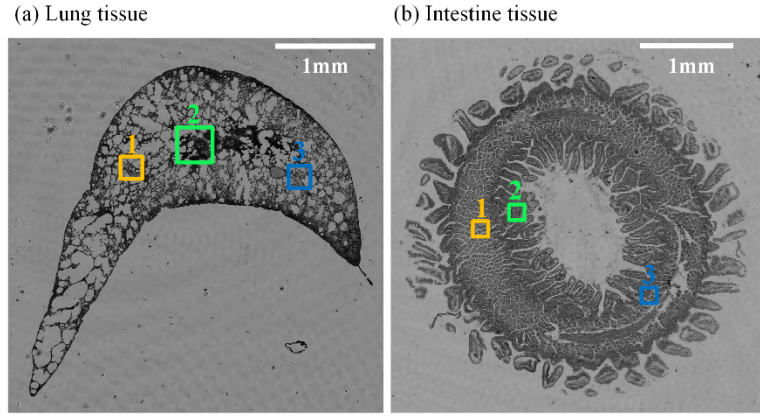


Fig. S7. The whole-field reconstructed images of lung and intestine tissues.

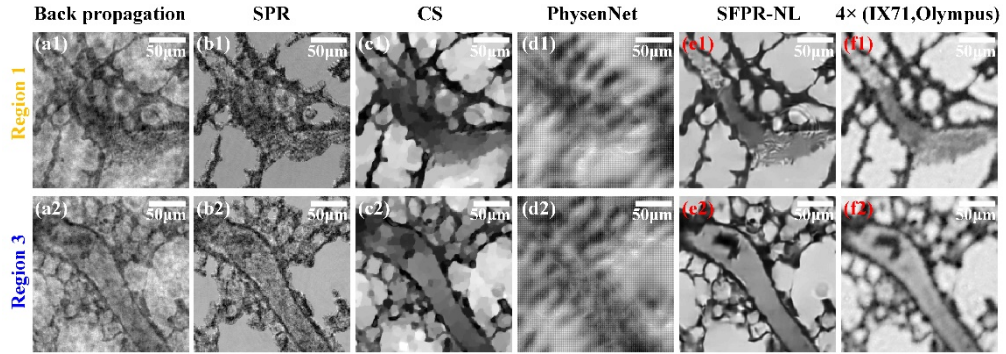


Fig. S8. The reconstructed results of selected regions from Fig. S7(a).

We provide the whole-field reconstructed amplitude images of H&E stained lung and intestine tissue in Fig. S7(a) and Fig. S7(b). The results related to region 2 of Fig. S7(a) have been displayed in the manuscript (Fig. 5). The results of region 1 and 3 are offered in Fig. S8. The retrieved images of intestine tissue are presented in Fig. S9. From Fig. S8 and Fig. S9, we can find that the reconstruction quality of our method is still superior to other methods.

Fig. S10 is the retrieved results for another group of stained breast tissue, which are also measured in the lensless multi-height system. In the experiment, 11 holograms with different sample-to-sensor distances are fed to multi-height phase retrieval to generate the ground truth images, which are given in Figs. S10(f1-f3). The hologram at the first height is used for single-frame image recovery. As shown in Fig. S10, the SSIM values of our method are larger than those of other methods, which indicates that our method has a better reconstruction accuracy.

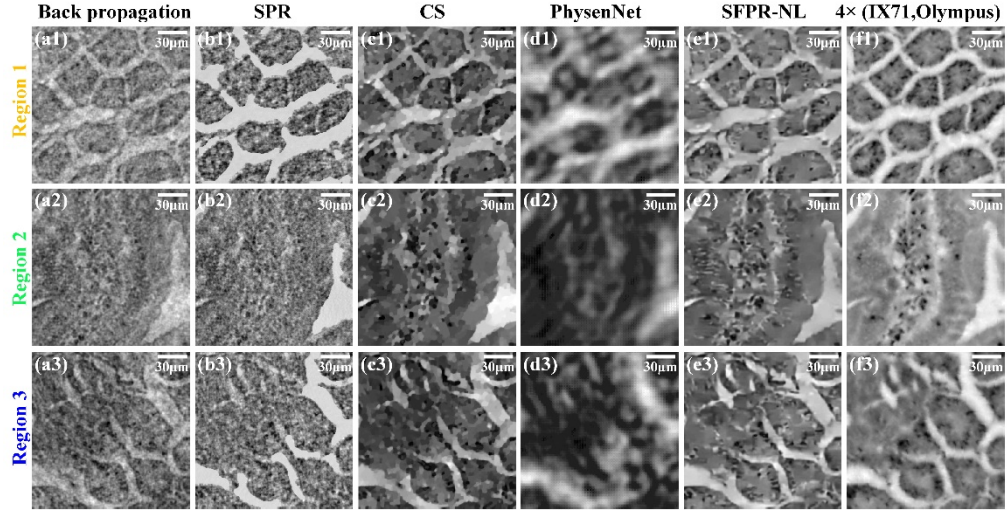


Fig. S9. The reconstructed results of selected regions from Fig. S7(b).

Back propagation	SPR	CS	PhysenNet	SFPR-NL	Multi-height phase Retrieval ($N=11$)
(a1) SSIM=0.573	(b1) SSIM=0.545	(c1) SSIM=0.599	(d1) SSIM=0.428	(e1) SSIM=0.799	(f1)
(a2) SSIM=0.589	(b2) SSIM=0.562	(c2) SSIM=0.597	(d2) SSIM=0.441	(e2) SSIM=0.814	(f2)
(a3) SSIM=0.629	(b3) SSIM=0.633	(c3) SSIM=0.628	(d3) SSIM=0.519	(e3) SSIM=0.802	(f3)

Fig. S10. The comparison of reconstructed accuracy for different single-frame methods.

Comparison of our method and multi-wavelength phase retrieval

We compare our method with multi-wavelength phase retrieval and offer the results in Fig. S11. The experiment of multi-wavelength imaging is conducted in the portable system (Fig. 2). A white LED is used as an illuminating source, and red, green, blue filters (FL632.8-1, FL532-1, FL488-1, FWHM = $1 \pm 0.2\text{nm}$, Thorlabs) are successively installed for quasi-monochromatic illumination. In data acquisition, a label-free microglia cell slide is chosen as the sample and only one hologram is captured at each wavelength. The histograms of multi-wavelength holograms are plotted in Figs. S11(a-c), where the recorded hologram at each wavelength is also inserted in the figure. Note that the brightness of red and blue holograms is obviously weaker than that of the green hologram. This unbalanced brightness is attributed to the fact that

the green channel takes a large proportion of the white LED spectrum. In data processing, three holograms are run by multi-wavelength phase retrieval methods (Ref. [5] and Ref. [6]), and the corresponding phase images are reconstructed in Fig. S11(g) and Fig. S11(h). The unbalanced multi-spectral illumination introduces extra noise for image recovery. Thus, in Fig. S11(g) and Fig. S11(h), the retrieved microglia cell is covered with a noisy background. In contrast, our method does not need multi-spectral holograms but utilize single-wavelength hologram for image recovery. Accordingly, the phase images related to red, green, and blue holograms are reconstructed by our method in Figs. S11(d-f). By contrast with Fig. S11(g) and Fig. S11(h), the results of our method show an enhanced imaging contrast of phase reconstruction. Figs. S11(d-i) are cropped from the region with a size of 1024×1024 . As the region is used for image recovery, the computing time of Ref. [5], Ref. [6], and our method is 10s, 14s, and 766s for this unstained cell. Compared to the methods in Ref. [5] and Ref. [6], our method increases computation complexity and running time. But our method does not need a multi-wavelength light source so the cost of lensfree microscope can be further decreased. This experiment demonstrates that our method achieves data-efficient and noise-robust image reconstruction.

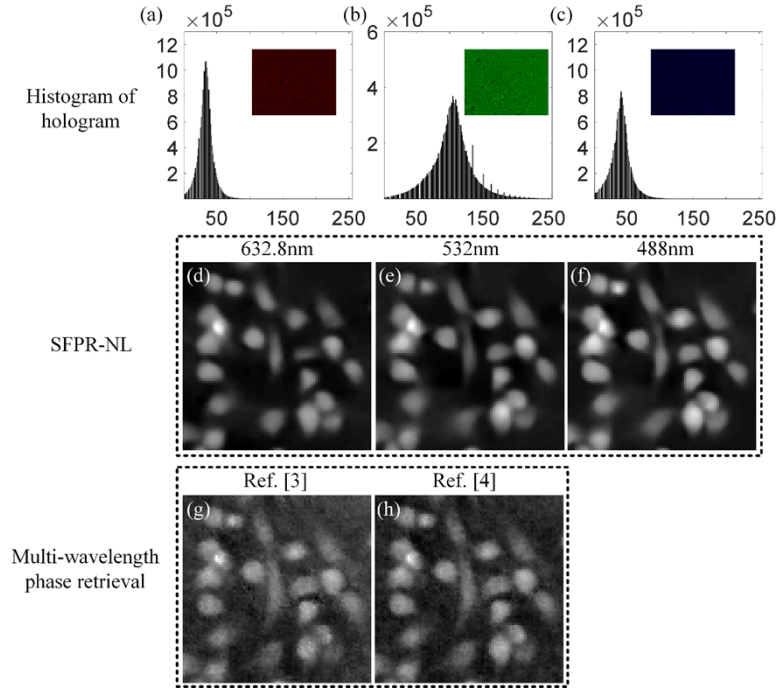


Fig. S11. The comparison of our method and multi-wavelength phase retrieval. (a-b) Histograms of the captured holograms with the illuminating wavelength of 632.8nm, 532nm, and 488nm. (d-f) Reconstructed phase images of our method for each wavelength. (g-h) Reconstructed phase images of multi-wavelength phase retrieval using three holograms.

References

1. I. M. Gelfand and V. A. Fomin, translated and edited by R. A. Silverman, *Calculus of Variations* (Dover, 2000).
2. D. H. Brandwood, "A complex gradient operator and its application in adaptive array theory," *IEEE Proc., Part H: Microwaves, Opt. Antennas* 130(1), 11–16 (1983).
3. Y. Zhang, Y. Shin, K. Sung, S. Yang, H. Chen, H. Wang, D. Teng, Y. Rivenson, R. P. Kulkarni, and A. Ozcan, "3D imaging of optically cleared tissue using a simplified CLARITY method and on-chip microscopy," *Sci. Adv.* 3, e1700553 (2017).
4. J. R. Fienup, "Invariant error metrics for image reconstruction," *Appl. Opt.* 36(32), 8352–8357 (1997).
5. P. Bao, F. Zhang, G. Pedrini, W. Osten, "Phase retrieval using multiple illumination wavelengths," *Opt. Lett.* 33(4), 309–311 (2008).

6. M. Sanz, J. A. Picazo-Bueno, J. García, and V. Micó, "Improved quantitative phase imaging in lensless microscopy by single-shot multi-wavelength illumination using a fast convergence algorithm," *Opt. Express* 23(16), 21352-21365 (2015).